# A Compact Broadband Frequency Selective Microstrip Antenna and Its Application to Indoor Positioning Systems for Wireless Networks

*Mustafa S. Bakr*[1,2,4], *Bernhard Großwindhager*[1], *Michael Rath*[1], *Josef Kulmer*[1], *Ian C. Hunter*[2], *Raed A Abd-Alhameed*[3], *Klaus Witrisal*[1], *Carlo Alberto Boano*[1], *Kay Römer*[1], *and Wolfgang Bösch*[1]

[1] Graz University of Technology, Inffeldgasse 8010, Graz, Austria
[2] Institute of Pollard, The University of Leeds, Leeds, UK
[3] School of Electrical Engineering, University of Bradford, UK
[4] Department of Electrical Engineering, University of Technology, Baghdad, Iraq
* E-mail: m.s.a.bakr@leeds.ac.uk; m7baker.ms@gmail.com

**Abstract:** This paper presents a low profile broadband microstrip patch antenna with filtering response. The proposed antenna consists of a rectangular patch and four parasitic gap-coupled elements, two L- and two rectangular-shaped patches. The broadband performance is realised by adjusting the height of the substrate, the length of the parasitic elements and the gaps between the rectangular patch and the parasitic elements. The filtering response is obtained by matching the input impedance of each radiating element, i.e., the driven patch and the four parasitic elements, to its radiation quality factor. This is done by optimising the substrate height, the width of each patch and the couplings between multiple resonators. The proposed antenna exhibits a broadband quasi-elliptic boresight gain response without using any extra filtering circuits. A prototype hardware is designed and fabricated on Kappa 438 substrate with a relative permittivity of 4.4 and thickness of 3.2 mm. The antenna exhibits a total size of $25 \times 23 \times 3.2$ mm with relative impedance bandwidth (VSWR<2) of 60% ranging from 4.4 to 7.8 GHz. The experimental results demonstrate good performance with nearly flat gain and good filtering response. The proposed filtering antenna exhibits low pulse distortion in time domain which makes it a good candidate for location-aware Internet-of-Things applications employing the IEEE 802.15.4 ultra-wideband (UWB) standard. Switchable sector indoor base-station antenna system is studied to demonstrate the capability of this design to enhance the localisation and communication performance of the wireless network.
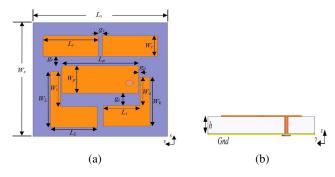
## 1 Introduction

As wireless communication systems evolve, there is much more emphasis being placed on the size, cost and performance of radio frequency front-ends. Filters and antennas are essential part of the wireless communication systems. They are separate components which occupy their own individual space and manufacturing cost. Conventionally, antennas and filters are connected by a matching network with a common reference impedance. Improper impedance matching can lead to excessive power loss, degrade the quality of the system and introduce signal interferences [1]. Thereafter, combining filters and antennas in the form of a single component is an effective method to reduce the size, loss and cost of wireless transceivers.

In recent years, significant efforts have been made to co-design filters and antennas as a single module, i.e., filtering antenna. A typical method to co-design filters and antennas is to replace the last resonator of a bandpass filter with a radiating element [2]. The well-known coupled-resonator filter theory is mainly used to design those components [3, 4]. Another classical method is to integrate the filtering circuits in the antenna radiating elements or its feeding networks [5]. However, the addition of extra filtering circuits can lead to an increase in the insertion loss, degrade the antenna radiation performance, and limit its operating bandwidth. This problem can be alleviated by designing filtering antennas without any filtering circuits. One way to achieve this is by matching the input impedance of the radiating element, named external quality factor ($Q_e$), to its radiation quality factor ($Q_r$). Alternatively, extra circuits, such as parasitic strips, shoring pins, etc., can be used to alter the excitation current path at defined frequencies and create nulls in the main radiation direction. In [6], a multilayer patch antenna with shorting pins is proposed to design filtering antennas without filtering circuits. Three

shorting pins and an etched slot were embedded in the driven patch to improve the out-of-band suppression levels and introduce nulls in the main radiation direction. However, the proposed filtering antenna is limited in bandwidth with an increase in the design complexity and fabrication cost. A single patch filtering antenna is introduced in [7]. The filtering performance is obtained by etching slots in a coaxial fed rectangular patch. However, the filtering antenna demonstrated suffers from limited bandwidth and big footprint for certain newly emerging applications such as compact indoor base stations, wearable devices and the Internet of Things.

The present work describes the design of a compact broadband microstrip filtering antenna without any extra filtering circuits, shorting pins or etched slots, covering a relative impedance bandwidth of 60% ranging from 4.4 to 7.8 GHz. The aim of introducing the filtering functionality in the antenna performance is to remove the need for the design of a filter that is immediately adjacent to the antenna and maximise the power transfer since no matching network is required. The proposed antenna consists of four parasitic elements, two L- and two rectangular-shaped patches, which are incorporated along the radiating and non-radiating edges of a probe feed rectangular patch. The broadband response is obtained by optimising the gaps between the multiple resonators. The filtering functionality is realised without using any extra circuits. In addition to the broadband response achieved by adding parasitic elements, they introduce radiation nulls on both sides of the gain response, thus; improve the out-of-band attenuation response. This is achieved by matching the input impedance of the antenna (expressed in $Q_e$) to its radiation output (expressed in $Q_r$). A prototype of the filtering antenna is designed, fabricated and measured to validate the proposed approach. The measured results demonstrate good performance. The motivation behind this work is to develop a low cost

directional switchable sector base-station filtering antenna system covering channels 3, 5 and 7 of the commercial UWB transceiver Decawave DW1000. The developed sector antenna can improve energy efficiency, reduce multi-user interferences, increase throughput and communication range with no significant energy cost as well as achieve highly accurate localisation performance [8].
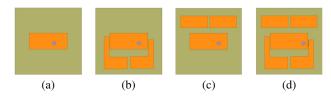
## 2 Antenna Design



**Fig. 1**: Configuration the proposed broadband microstrip filtering antenna with L- and rectangular-shaped parasitic elements. (a) Top view. (b) side view.

The configuration of the proposed broadband microstrip filtering antenna is depicted in Fig. 1. Its geometry is specified in Table 1. The antenna is printed on top of Kappa 438 substrate with a relative permittivity of 4.4, tan($\delta$) of 0.005, and thickness (h) of 3.2 mm. On the bottom side, a conducting ground is printed to minimise radiation in the back lobe direction. The four parasitic elements (two L- and two rectangular shaped-parasitic elements) are placed along the radiating and non-radiating edges of the main rectangular patch- named the driven patch. The driven patch width ($W_p$) is reduced to $\lambda_l/4.6$ and its length ($L_p$) is about $\lambda_l/2$ - corresponding to approximately 5.13 GHz, where $\lambda_l$ is the guided wavelength. A coaxial probe is applied via a vertical hole in the substrate to feed the driven patch. The four parasitic elements are positioned with near proximity to the driven patch contributing to the antenna impedance bandwidth enhancement through electromagnetic coupling (i.e., EM coupling between multiple resonances). The driven patch and parasitic elements operating mode is the $TM_{10}$ mode.
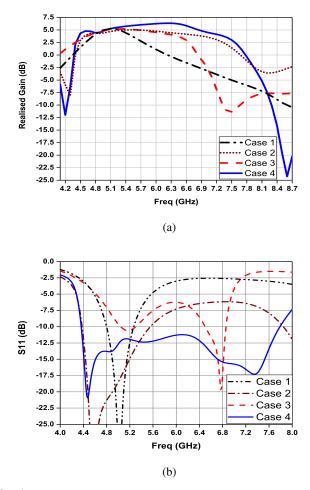
**Table 1** The geometrical parameters of the proposed antenna.

| | | |
|---|---|---|
| $L_s$ = 25 mm | $W_s$ = 23 mm | $L_p$ = 13.1 mm |
| $W_p$ = 6 mm | $W_L$ = 12.25 mm | $L_L$ = 8 mm |
| $W_r$ = 4.5 mm | $L_r$ = 9.4 mm | $W_i$ = 6 mm |
| $W_o$ = 6.25 mm | $W_k$ = 10.75 mm | $L_i$ = 6.25 mm |
| $g_p$ = 0.25 mm | $g_r$ = 1.9 mm | $g_v$ = 2.5 mm |
| $g_i$ = 2.75 mm | h = 3.2 mm | |

The proposed antenna was simulated and optimized using a frequency domain three-dimensional full-wave electromagnetic solver Ansoft HFSS. As depicted in Fig. 2, four cases have been simulated to define the design procedure of the enhanced bandwidth microstrip antenna with filtering functionality; Case 1 shows the driven patch alone before adding the parasitic elements, case 2 defines the effect of adding the L-shaped parasitic elements, case 3 shows the performance of the array after adding the two rectangular parasitic elements and case 4 shows the overall antenna performance after adding all of the parasitic elements. In case 1, the microstrip patch antenna has a relative impedance bandwidth of 10.5% over which $S_{11} \leq$ -10 dB. The $S_{11}$ of the rectangular patch before adding the parasitic elements is shown in Fig. 3. The boresight gain response vs frequency shows slow band skirt despite the fact that the antenna



**Fig. 2**: The procedure of adding the parasitic elements to improve the antenna bandwidth performance in which case 1 is shown in (a), case 2 in (b), case 3 in (c), case 4 in (d).



(a)



(b)

**Fig. 3**: Simulated reflection coefficient and broadside gain of the proposed antenna for the four cases (a) Broadside gain (b) reflection coefficient.

input impedance was optimised to match its radiation quality factor. The antenna impedance bandwidth is comprised between 4.7 to 5.2 GHz. In case 2, the presence of the two L-shaped parasitic elements shift the lower frequency bound of the main rectangular patch due to their total physical lengths. The resonant frequency of the L-shaped patches is controlled by adjusting its length ($L_L$ and $L_i$) and width ($W_L$, $W_i$, $W_o$, and $W_k$). The L-shaped patches are designed to resonate at 4.5 and 4.9 GHz. The antenna impedance bandwidth is extended from 4.47 to 5.5 GHz with nearly flat boresight gain response vs frequency and one radiation null at the low side as shown in Fig. 3. In case 3, the rectangular-shaped parasitic patches shift the higher frequency bound of the main rectangular patch antenna by contributing two resonances at 6.5 and 6.7 GHz. The resonant frequencies are controlled mainly by adjusting the length ($L_r$) of each patch while the radiation quality factor is optimised by adjusting the width ($W_r$). The -6 dB antenna impedance bandwidth is extended from 4.74 to 7 GHz with nearly flat gain and one radiation null at
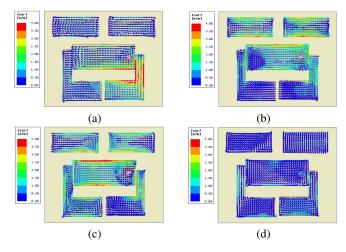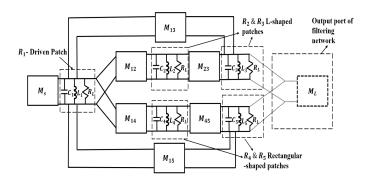
**Fig. 4**: Simulated surface current of the proposed antenna at (a) 4.7GHz, (b) 6.5 GHz, (c) 7.5 GHz, and (d) 8.615 GHz .

the high side as shown in Fig. 3. In case 4, the four parasitic elements are added in close proximity to the main rectangular radiating patch contributing to the antenna impedance bandwidth and filtering response. The boresight gain exhibits sharp band skirt response with two radiation nulls, one on each side. This is achieved by careful optimization of the vertical ($g_i$ and $g_r$) and horizontal ($g_p$ and $g_v$) gaps between the main rectangular patch and the parasitic elements. The position of the coaxial probe was optimized to achieve the maximum impedance matching in the four different cases. The substrate height, and the width of the driven patch and parasitic elements were optimised to achieve good filtering response in the antenna main radiation direction. The specific values of the five coupled resonant frequencies are found to be 4.5, 4.9, 5.13, 6.5, and 6.7 GHz.

The current distribution of the proposed antenna is simulated at the resonant frequencies of one of the L- and rectangular-shaped parasitic elements respectively (4.7, and 6.5 GHz), near the upper bound of the antenna impedance bandwidth (7.5 GHz), and at the frequency of the upper radiation null (8.615 GHz). It is evident from the simulation results shown in Fig. 4 that the driven patch is mainly coupling to the L-shaped parasitic elements at lower frequencies, i.e. 4.5, 4.9 GHz, contributing to the enhancement of the antenna impedance bandwidth at the lower bound as well as radiation performance. Similarly, the driven patch is mainly coupling to the rectangular-shaped parasitic elements at upper frequencies, i.e. 6.5, 6.7 GHz, contributing to the enhancement of the antenna impedance bandwidth at the upper bound as well as radiation performance. This contributes to the broadband response of the proposed antenna. The driven patch is minimally coupling to any of the parasitic elements at its resonant frequency, 5.13 GHz. This leads to good radiation performance via frequency due to small couplings between the different parasitic elements off-resonance. At frequencies near the upper frequency bound, the driven patch is coupling to the four parasitic elements; thus, exciting the first higher order mode of the L-shaped parasitic elements. This degrades the radiation performance of the proposed antenna at higher frequencies. The simulation result at the frequency of the high radiation null, i.e. 8.615 GHz, has minimum surface current; thus, contribute to nearly no radiation and good out-of-band rejection levels.
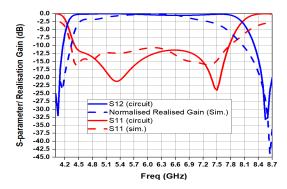
## 3 Circuit Model

The proposed antenna structure consists of five coupled resonators with each resonator acting as a radiation output. Its circuit model is depicted in Fig. 5. All resonators in Fig. 5 - named $R_1$ (driven patch), $R_2$ & $R_3$ (L-shaped patches) and $R_4$ & $R_5$ (rectangular-shaped patches)- are modelled as parallel RLC resonators at their resonant frequencies. The feeding probe ($M_s$) is modelled as a series inductor. The couplings between the driven patch and the parasitic elements ($M_{12}$, $M_{13}$, $M_{23}$, $M_{14}$, $M_{15}$ and $M_{45}$) are modelled



**Fig. 5**: Circuit model of the proposed antenna where the output port (dotted lines and $M_L$) is added when the filtering network response is calculated ($S_{12}$).
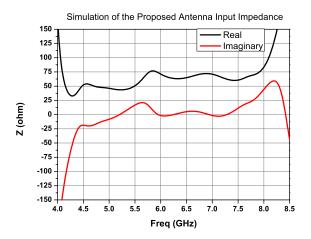
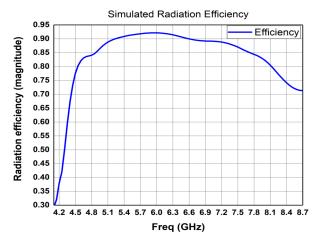as reactances. The filtering functionality is introduced by optimis-



**Fig. 6**: Simulation and theoritical reflection/transmission coefficients and normalised realised gain of the proposed antenna

ing the input to resonator coupling ($M_s$), radiation quality factor ($Q_r$)- defined as $R_L$ in the circuit model shown in Fig. 5, and the coupling coefficients between the multiple resonators ($M_{ij}$)- i.e. radiating patches (see Fig. 5). The antenna filtering performance is improved by introducing finite transmission zeros near the bandpass edges as shown in Fig. 6. The finite transmission zero (radiation null) on the lower side of the bandpass edge (boresight gain response) is related to $M_{12}$, $M_{23}$, and $M_{13}$ couplings, i.e., coupling ratios between the driven patch and L-shaped parasitic patches. Similarly the finite transmission zero (radiation null) on the upper side of the bandpass edge (boresight gain response)is related to $M_{14}$, $M_{45}$, and $M_{15}$ couplings, i.e., coupling ratios between the driven patch and rectangular-shaped parasitic patches.

Fig. 6 shows the simulation results of the circuit model (Fig. 5) and EM model (Fig. 1) of the antenna where the red lines represent the $S_{11}$ response, solid blue line represents the $S_{12}$ of the corresponding filter model- i.e. $R_3$ and $R_5$ are connected to each other and then terminated in 50 ohm port. In other words, two ports network. The dashed blue line represents the normalised realised gain of the EM model. The simulation results of $S_{12}$ is slightly different from the antenna normalised realised gain around the bandpass edges since no losses considered in the corresponding filter model. When the proposed antenna is properly matched, the real part of input impedance of the circuit and EM simulation results fluctuates between 30 ohm and 75 ohm. The imaginary part of the input impedance fluctuates between -25 ohm to 25 ohm and therefore, it appears that there is no need to use another technique to tune out the probe inductance to allow matching (Fig. 7). The antenna radiation efficiency is better than 83% in-band and drops rapidly out-of-band due to the location of radiation nulls near the band-edges and the fact that the antenna is optimised to exhibit filtering response, shown in Fig. 8.

**Fig. 7**: Simulated Response of real and imaginary part of the antenna input impedance.



**Fig. 8**: Simulated Response of the radiation efficiency of a proposed patch antenna antenna.



**Fig. 9**: Simulated reflection coefficients and realised gain for different sizes of substrate height.



**Fig. 10**: Simulated reflection coefficients and realised gain for different positions of feeding probe.
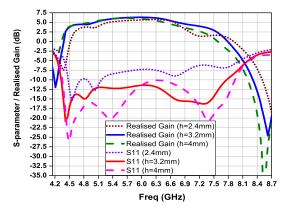
## 4 Parametric Study

A parametric study of the proposed filtering antenna, mostly covering channel 3, 5 and 7 of DW1000 (4.3 to 7.8 GHz), was carried out using Ansoft HFSS simulator. The characterisation of the antenna is summarised as follow:
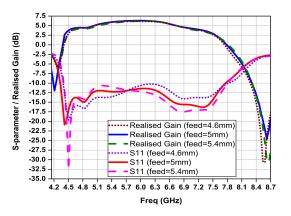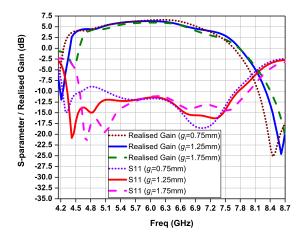
### 4.1 Effect of the substrate height

The effect of the substrate height on the filtering antenna performance is studied first. Fig. 9 shows the simulated reflection coefficients and boresight gains for different substrate heights. It can be seen that as the substrate height increases, the impedance bandwidth increases. This is expected because a larger substrate height leads to a decrease in the antenna quality factor [9]. However, this does not guarantee nearly flat gain response. The antenna reflection coefficients and gains as a function of substrate height have to be optimised simultaneously to guarantee good electrical performance. The optimal value of the substrate height for this antenna is found to be 3.2mm.

### 4.2 Effect of the feeding position

The effect of adjusting the feeding position along the non-radiating edges is shown in Fig. 10. It is apparent that the feed location has nearly no effect on the gain response and the locations of radiation nulls. It mainly influence the impedance matching performance.

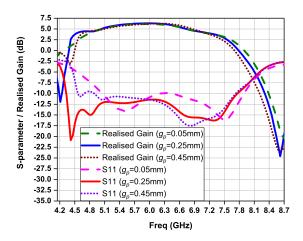### 4.3 Effect of the distance between the driven patch and L-shaped patches

The effect of adjusting the distance between the driven patch and the L-shaped patches, named $g_i$ and $g_p$, is studied. As shown in Fig. 11 and Fig. 12, the lower frequency bound of the reflection coefficients and gains responses are affected significantly as $g_i$ and $g_i$ vary from 0.75 to 1.75mm and 0.05 to 0.45mm respectively. It can be found that as the distance between the driven patch and two L-shaped patches gets smaller $g_i$ along the y-axis, the coupling between them gets higher; thus, shifts the locations of the radiation null away from the lower band edge. Similarly, as the distance between the driven patch and the L-shaped patches gets smaller along the x-axis, i.e., higher input to resonator couplings from the L-shaped patches point of view, the radiation nulls migrate away from the lower band edge. Careful optimisation of $g_i$ and $g_p$ are required to position the radiation null at the desired frequency, maintain good impedance matching and flat gain response at the lower bandedge.

### 4.4 Effect of the distance between the driven patch and rectangular-shaped patches

The effect of adjusting the distance between the driven patch and the rectangular-shaped patches, named $g_v$ and $g_r$ is investigated. As shown in Fig. 13 and Fig. 14, the upper bound reflection coefficients and gains responses are affected significantly as $g_v$ and $g_r$ vary from 0.25 to 2.25mm and 1 to 3mm respectively. It can be found that as the distance between the two rectangular-shaped patches gets smaller

**Fig. 11**: Simulated reflection coefficients and realised gain for different gap separation of L-shaped parasitic elements and driven patch ($g_i$).



**Fig. 13**: Simulated reflection coefficients and realised gain for different gap separation between rectangular parasitic elements ($g_v$).
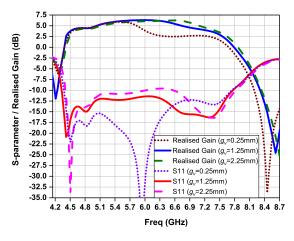


**Fig. 12**: Simulated reflection coefficients and realised gain for different gap separation of L-shaped parasitic elements and driven patch ($g_p$).



**Fig. 14**: Simulated reflection coefficients and realised gain for different gap separation of rectangular parasitic elements to driven patch ($g_r$).
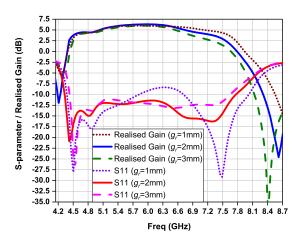
$g_v$, the coupling between them gets higher; thus, shifts the locations of the radiation null closer to the upper bandedge. On the contrary, as the distance between the driven patch and the rectangular-shaped patches gets smaller, i.e., higher input to resonator couplings from the rectangular-shaped patches point of view, the radiation nulls migrate away from the upper band edge. Careful optimisation of $g_v$ and $g_r$ are required to position the radiation null at the desired frequency, maintain good impedance matching and flat gain response at the upper bandedge.

### 4.5 Effect of the ground size

The effect of adjusting the ground size is explored in this section. The size of the ground plane is increased from $23 \times 25$mm to $33 \times 35$mm. The filtering antenna gain and back lobe performance are improved at the upper frequency bound as the ground size increases. In addition, the location of the radiation null on the high side is moved close the upper band-edge as the ground siz increases. This results in improved radiation and out-of-band performance at the expense of total size. The degraded radiation response at higher frequencies is caused by field diffraction at the edges of the ground plane in which the electric field distribution becomes discontinuous.

The severity of this phenomenon can be reduced by increasing the separation between the different patches and ground edges; thus, better radiation performance. Fig. 16 shows the radiation performance at 7.2 GHz as a function of ground size. The impedance matching and realised gain response is shown in Fig. 15.

### 4.6 Design Rules

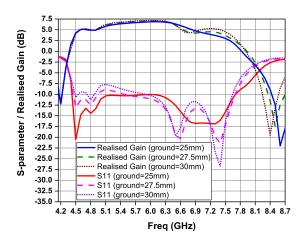Based on the above parametric study, a design guideline is recommended as follows:

1. First, set the dimensions of the driven and parasitic patches near the lower, upper and centre frequency of the given specifications.
2. Optimise the height of the substrate and the width of each patch to achieve nearly flat gain with filtering response.
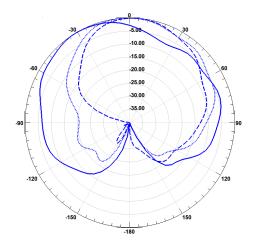3. Optimise the location of the feeding probe for optimum broadband impedance matching.
4. Optimise the gaps between the driven patch and parasitic elements to improve the impedance matching performance, gain flatness, and position of radiation nulls.
5. Optimise the ground plane size for better radiation performance and re-optimise 3 until the desired impedance matching is met.

**Fig. 15**: Simulated reflection coefficients and realised gain as a function of ground size.



**Fig. 16**: Simulated radiation pattern at 7.2 GHz for different increase of ground size as follows: solid line (0mm), dotted line (5mm), and dashed line (10mm).
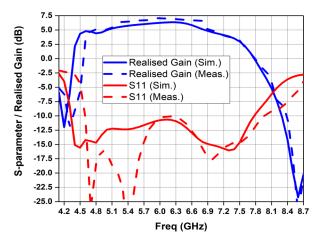
## 5 Results and Analysis

The antenna was fabricated using a chemical etching process. Fig. 17 shows the fabricated prototype of the proposed antenna. The fabricated antenna was measured using the anechoic chamber at Bradford University. Fig. 18 shows a good agreement between the simulation



**Fig. 17**: Photograph of the fabricated proposed antenna.

and measured reflection coefficient ($S_{11}$ in dB) and realised gain of the proposed antenna. The simulated impedance bandwidth ranges from 4.4 to 7.8 GHz with a fractional bandwidth of 60%. In comparison to the simulation results, the measured impedance bandwidth is displaced by approximately 0.2 GHz ranging from 4.6 to 8 GHz with a fractional bandwidth of 60%. This shift in impedance bandwidth

is believed to originate from inaccuracies due to the manual process of manufacture of the prototype. The antenna simulation and measured radiation patterns (co and cross-polarization components) at four frequencies (4.7, 5.5, 6, and 7.5 GHz) are depicted in Fig. 19. The measured radiation characteristics of the proposed antenna are



**Fig. 18**: Simulated and measured reflection coefficients and realised gain of the proposed antenna.
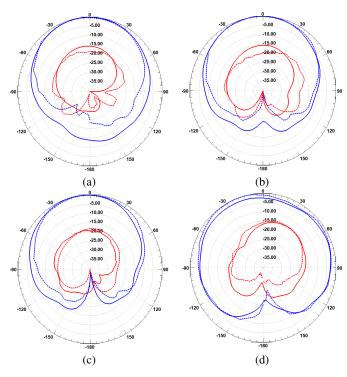
notably similar to a conventional microstrip patch antenna with a maximum measured gain of 7.2 dB at 6 GHz. Fig. 19 shows that the antenna exhibits minimum beam tilt with frequency. The tilt with frequency is caused by the asymmetry of the structure. The moderate gain and back lobe performance at higher frequencies are caused by the small size of the ground place. This can be improved by increasing the ground plane size as discussed in section 4.5. Table 2 shows a summary of the antenna performance at nine frequencies. A comparison between the proposed antenna and the state of the art compact directional wideband antennas in terms of size, bandwidth and maximum gain is show in Table 2. The proposed antenna outperforms the selected state of the art antennas in terms of size, which is a necessary requirement for pervasive applications in the IoT domain.

**Table 2** Summary of the Antenna Performance.

| Freq. (GHz) | Sim. Rad. efficiency (%) | Sim. HPW (deg.) | Meas. HPW (deg.) | Sim. realised gain (dB) | Meas. realised gain (dB) |
|---|---|---|---|---|---|
| 4.7 | 83.6 | 98 | 95 | 4.72 | 5.2 |
| 5 | 87.4 | 95 | 90 | 5 | 5.1 |
| 5.5 | 91.3 | 91 | 92 | 5.84 | 6.5 |
| 5.8 | 92 | 90 | 95 | 6.2 | 6.7 |
| 6 | 92.2 | 91 | 94 | 6.4 | 7.2 |
| 6.5 | 90.5 | 88 | 84 | 6.2 | 6.8 |
| 7 | 89.2 | 98 | 80 | 4.5 | 4.8 |
| 7.2 | 88.8 | 120 | 98 | 4.2 | 4.5 |
| 7.5 | 87 | 160 | 164 | 3 | 3.5 |

## 6 Antenna Characteristics for UWB Applications

In UWB applications, unlike narrowband communications, the antenna transmits or receives signal with extremely narrow pulses on the order of 1ns or less resulting in bandwidths of excess of 500 MHz. Thus the effect of pulse distortion is more obvious in UWB applications. Therefore, It is a requirement to design antennas that produce minimum pulse distortion in time domain. CST Microwave Studio is used to analyse the proposed antenna usability for UWB applications. A number of electric field probes are placed in the far field region, a distance of 230mm away of the antenna, with different radiation directions as shown in Fig. 20.

**Fig. 19**: Simulated and measured radiation patterns where solid and dashed blue lines represent simulated and measured co-polarisation (xz-plane) respectively: (a) 4.7 GHz, (b) 5.5 GHz, (c) 6 GHz, and (d) 7.5 GHz.

**Table 3** Comparison of State-of-the-Art directional wideband antennas.

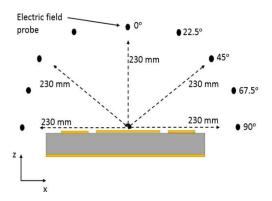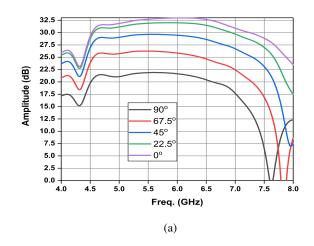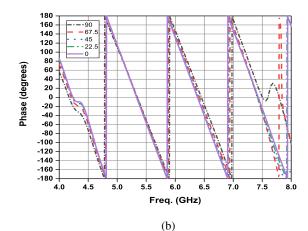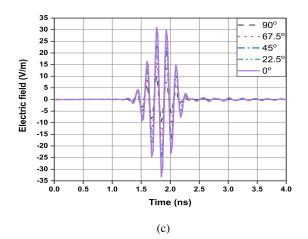| Reference no. | Dimensions (mm × mm × mm) | Centre freq. $f_0$ | BW (%) | Max. Gain (dB) | Filtering technique |
|---|---|---|---|---|---|
| This work | 23 × 25 × 3.2 | 5.85 | 60 | 7.2 | parasitic elements |
| [7] | 45 × 45 × 1.524 | 5.24 | 7 | 6.6 | slots |
| [10] | 78 × 78 × 3.813 | 5 | 28.4 | 8.2 | slots, shorting via |
| [11] | 28 × 28 × 15 | 4.63 | 74 | 8.5 | |
| [12] | $0.5\lambda \times 0.5\lambda \times 0.508$ | 5 | 2 | 4 | filtering circuit |
| [13] | 50 × 50 × 5.77 | 3.98 | 48 | 5 | |



**Fig. 20**: Side view of the proposed antenna showing electric field probes.

The magnitude of the antenna transfer function in different directions is shown in Fig. 21(a). The direction 0° refers to radiation perpendicular to the antenna surface, bore-sight radiation direction. Similarly, the direction 90° refers to end-fire radiation direction. The
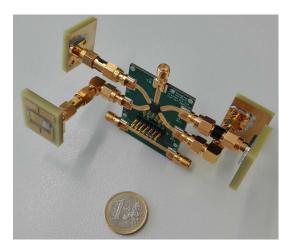


(a)



(b)



(c)

**Fig. 21**: Simulations responses of the proposed antenna (a) amplitude (dB) in different propagation directions (b) phase (degrees) in different propagation directions and (c) radiation pulses (ns) in different propagation directions

results shown in Fig. 21 are for a dominant electric field component since the antenna is linearly polarised. The distance between the antenna and the electric field probes is 230 mm. It can be seen in Fig. 21(a) that the antenna transfer functions are nearly flat over the antenna impedance bandwidth for all directions. In addition, the antenna filtering performance is evident at the upper and lower edges of the passband where two finite transmission zeros are introduced to improve the filtering performance. The phase response of the antenna transfer function is shown in Fig. 21(b). The proposed antenna introduces minimum distortion to the transmitted

pulse response in all directions. In addition, the radiated pulse envelope in five directions is shown in Fig. 21(c). All pulses are very similar with minimum distortion. In other words, the duration of the ringing of the UWB antenna is negligibly small. These results confirm the usability of the proposed antenna for UWB applications.

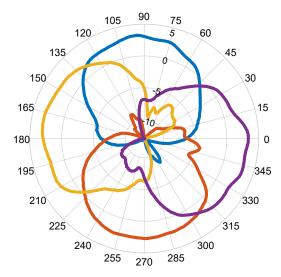# 7 Low Profile Switchable Sector Antenna for Low-Power Wireless Networks and IoT Applications

Despite the enormous potential of directional antennas [14, 15], the majority of the devices employed to build low-power wireless networks and IoT applications use omnidirectional antennas. Consequently, to reduce the amount of collisions in a network, only one device is allowed to transmit data at a given time. This results in a low spatial reuse of the channel, reduced network capacity, and increased network delays. UWB provides a high immunity to multipath fading due to the high resolution in delay domain [16]. Still, fluctuations of the received signal strength caused by shadowing and non-line-of-sight conditions lead to a drop in the quality of a wireless link. Multiple directional antennas overcome this issue by providing spatial and angular diversity; thus, in the case of a degraded wireless channel, switching to a different antenna supports maintaining a reliable link.



**Fig. 22**: Directional antenna system containing four antennas and the RF switching network [17].

This inspired the design of a switchable directional antenna system as shown in Fig. 22 [17]. It consists of a high-speed and low-power RF switching network (employing the UltraCMOS RF switch PE42441 from Peregrine Semiconductor) and four of the proposed directional antennas. The RF switching network is controlled via GPIO ports from a host processor. To ensure a seamless switching between the antennas, a switching time of a few $\mu$s was achieved. Fig. 23 shows the measured coverage of the four antennas in the xz plane at 5 GHz. The directional antenna system provides a proper $360°$ coverage: this is a necessary step to enable IoT applications in mobile and highly dynamic environments. The average gain of the antenna system is 3.728 dB and the half-power beamwidth is $98.5°$. The reduced gain in comparison to Fig. 19 is due to the losses in the switching network. Still, the achieved gain results in a increased communication range of UWB-based wireless devices and in a spatial reuse of the channel.

UWB transceivers enable high-accurate localization based on time-offlight (ToF) estimations. This requires low-distortion pulses and a separation of the direct path and reflected multipath components (MPC). In recent work, it was shown that even the ToF of MPCs can be exploited, reducing the required infrastructure and/or improving the robustness of the positioning system [18]. However, in unfavourable positions the MPCs might overlap, which makes them



**Fig. 23**: Measured radiation pattern of the switchable directional antenna system at 5 GHz (co-polarisation xz plane) [17].

unresolvable even at high bandwidth. The directionality of the proposed sector antenna can overcome this issue by utilising the angular domain to improve the system robustness against MPC overlap. To demonstrate this capability, measurements were performed using the proposed sector antenna as receiver and an omnidirectional antenna as transmitter. The measurement setup was carried out with a centre frequency of $f_c = 5.5$ GHz and a bandwidth of 500 MHz. The distance between transmitter and receiver was increased as well as the observed time frame to analyse specular reflections and diffuse multipath propagation effects. The transmitter moved at a $10 \times 10$ grid with spacing of 5 cm, resulting in 100 measurements. Both antennas were placed indoors in a room with dimensions of $6 \times 8$ m under line-of-sight (LOS) conditions. For comparison, the experiment was repeated with an omnidirectional antenna on both the transmitter and receiver sides. The received signal at the proposed antenna can be decomposed in a line-of-sight (LOS) followed by two reflections, denoted as R1 and R2. The expected delay of the LOS is $\tau_{LOS} = 11.1$ ns and the delays of both reflections are $\tau_{R1} = 15.0$ ns and $\tau_{R2} = 16.6$ ns. The delays were calculated using building plans where influences like diffraction or penetration were neglected. The delay difference of both MPCs is below the pulse duration, i.e. $|\tau_{R2} - \tau_{R1}| < T_p$, which will result in a path overlap. To get an insight into the antenna's ability of angular separation of the MPCs, the sector antenna was steered such that the mainlobe points to the angles of individual MPCs, i.e., the measurements were repeated by switching the sector antenna in the direction of the LOS followed by R1, and R2. The angles of arrival are fairly separated in the angular domain ($\theta_{R1} = -94°$ and $\theta_{R2} = 109°$ for $\theta_{LOS} = 0°$). Fig. 24 shows the measurements carried out at one transmitter position. The proposed sector antenna performance is compared with equivalent omnidirectional antenna. In the omnidirectional antenna case, it can be observed that the LOS is well separated in time domain. Both reflections coincide and form a peak at approximately 15 ns. The shape of this superposition depends on the individual amplitudes and phases of both MPCs. Without additional information these parameters cannot be extracted, i.e., R1 and R2, using only the omnidirectional antenna. This is different with the sector antenna being used. Switching the mainlobe to a specific MPC enables the suppression of interfering MPCs that arrive at the same time, especially at R1 and R2 directions.

Signal-to-interference-and-noise ratio (SINR) was measured to complement the qualitative evaluation described previously. The SINR is a metric to assess the ranging information intensity of specific MPCs. It quantifies the energy ratio of a useful deterministic MPC to interfering diffuse multipath. The latter causes small-scale fading of the amplitude of a deterministic MPC. A high SINR refers
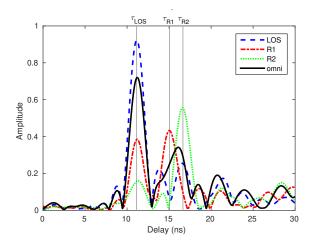
**Fig. 24**: Measured impulse response steering the antenna's main-lobe in the direction of the LOS (blue, dashed), reflection R1 (red, dotted dashed) and reflection R2 (green, dotted). The impulse response measured with an omnidirectional antenna (black, solid) is shown for comparison.

to little fading and hence the corresponding MPC will provide reliable position information. The SINR of a single MPC is estimated using method-of-moments, based on the amplitudes of the MPCs. Table **??** shows the achieved SINR values for different steerings of the sector antenna's mainlobe (first column) for the LOS, R1, and R2, each estimated from 100 measurements at different transmitter positions on the grid. The results for the omnidirectional antenna are shown for comparison. The SINR of the LOS attains the highest values justified by its isolation along the time domain. The SINRs of R1 and R2 are strongly dependent on the mainlobe steering. Switching the antenna in the direction of R1 or R2 strongly increases the SINR of the MPC arriving at $\tau_{R1}$ or $\tau_{R2}$. The SINRs of reflections R1 and R2, which cannot be resolved by the omnidirectional antenna due to massive path overlap . We can conclude that the proposed antenna is able to separate simultaneously arriving MPCs while preserving its favourable properties in time domain. In [18], algorithms and performance limits are discussed for the proposed antenna to enhance the accuracy and robustness of a multipath-assisted indoor positioning system, allowing for a reduction of the required signal bandwidth.

**Table 4** SINR (in dB) of the LOS and reflections R1 and R2 for various directions of the antenna's mainlobe.

| steered to arrival at | $\tau_{LOS}$ | $\tau_{R1}$ | $\tau_{R2}$ |
|---|---|---|---|
| LOS | 25.5 | -6.2 | 3 |
| R1 | 20.8 | 16.5 | $-\infty$ |
| R2 | 12.9 | -3 | 17.7 |
| Omni | 26.2 | 6.4 | 7.6 |

## 8    Conclusion

A novel wideband microstrip patch antenna with filtering functionality has been presented. L- and rectangular-shaped parasitic elements are incorporated along the radiating and non-radiating edges of a reduced-size rectangular patch to enhance the antenna impedance bandwidth. The parasitic elements are coupled to the main patch by adjusting the horizontal and/or vertical gaps between the main patch and the parasitic elements. The filtering functionality is introduced by using the the coupled-resonator filter design theory to match the antenna input to resonator coupling and the radiation output. The overall dimension of the proposed antenna is $23 \times 25 \times 3.2$ mm.

The measured antenna fractional bandwidth is 60% with nearly flat gain. The measured radiation patterns are quite similar to a conventional microstrip patch antenna with maximum measured gain of 7.2 dB at 6 GHz. The proposed antenna demonstrate minimum pulse distortion and excellent performance for UWB applications. Switchable sector antenna system, employing multiples of the proposed antenna, has been developed to enhance wireless communication and localization.

## Acknowledgment

## 9    References

1  Constantine A. Balanis. 2005. "Antenna Theory: Analysis and Design." Wiley-Interscience, New York, NY, USA.

2  J. Qian, F. Chen, Y. Ding, H. Hu and Q. Chu, "A Wide Stopband Filtering Patch Antenna and Its Application in MIMO System," in IEEE Transactions on Antennas and Propagation.

3  A. I. Abunjaileh, I. C. Hunter and A. H. Kemp, "A Circuit-Theoretic Approach to the Design of Quadruple-Mode Broadband Microstrip Patch Antennas," in IEEE Transactions on Microwave Theory and Techniques, vol. 56, no. 4, pp. 896-900, April 2008.

4  M. Kufa, Z. Raida and J. Mateu, "Three-Element Filtering Antenna Array Designed by the Equivalent Circuit Approach," in IEEE Transactions on Antennas and Propagation, vol. 64, no. 9, pp. 3831-3839, Sept. 2016.

5  X. Y. Zhang, Y. Zhang, Y. Pan and W. Duan, "Low-Profile Dual-Band Filtering Patch Antenna and Its Application to LTE MIMO System," in IEEE Transactions on Antennas and Propagation, vol. 65, no. 1, pp. 103-113, Jan. 2017.

6  X. Y. Zhang, W. Duan and Y. Pan, "High-Gain Filtering Patch Antenna Without Extra Circuit," in IEEE Transactions on Antennas and Propagation, vol. 63, no. 12, pp. 5883-5888, Dec. 2015.

7  J. Y. Jin, S. Liao and Q. Xue, "Design of Filtering-Radiating Patch Antennas With Tunable Radiation Nulls for High Selectivity," in IEEE Transactions on Antennas and Propagation, vol. 66, no. 4, pp. 2125-2130, April 2018.

8  M. Rath, J. Kulmer, M. S. Bakr, B. Großwindhager and K. Witrisal, "Multipath-assisted indoor positioning enabled by directional UWB sector antennas," 2017 IEEE 18th International Workshop on Signal Processing Advances in Wireless Communications (SPAWC), 2017, pp. 1-5.

9  D. H. Schaubert, D. M. Pozar and A. Adrian, "Effect of microstrip antenna substrate thickness and permittivity: comparison of theories with experiment," in IEEE Transactions on Antennas and Propagation, vol. 37, no. 6, pp. 677-682, Jun 1989.

10  Y. M. Pan, P. F. Hu, X. Y. Zhang and S. Y. Zheng, "A Low-Profile High-Gain and Wideband Filtering Antenna With Metasurface," in IEEE Transactions on Antennas and Propagation, vol. 64, no. 5, pp. 2010-2016, May 2016.

11  H. Nakano and J. Yamauchi, "Printed Slot and Wire Antennas: A Review," in Proceedings of the IEEE, vol. 100, no. 7, pp. 2158-2168, July 2012.

12  C. Lin and S. Chung, "A Compact Filtering Microstrip Antenna With Quasi-Elliptic Broadside Antenna Gain Response," in IEEE Antennas and Wireless Propagation Letters, vol. 10, pp. 381-384, 2011.

13  Nasimuddin and Z. N. Chen, "Multipatches multilayered UWB microstrip antennas," in IET Microwaves, Antennas & Propagation, vol. 3, no. 3, pp. 379-386, April 2009.

14  Dai, Hongning et al. "An overview of using directional antennas in wireless networks." Int. J. Communication Systems 26 (2013): 413-448.

15  G. Giorgetti, A. Cidronali, S. K. S. Gupta and G. Manes, "Exploiting Low-Cost Directional Antennas in 2.4 GHz IEEE 802.15.4 Wireless Sensor Networks," 2007 European Conference on Wireless Technologies, Munich, 2007, pp. 217-220.

16  A. F. Molisch, "Ultra-Wide-Band Propagation Channels," in Proceedings of the IEEE, vol. 97, no. 2, pp. 353-371, Feb. 2009.

17  B. Großwindhager, M. S. Bakr, M. Rath, F. Gentili, W. Bösch, K. Witrisal, C. A. Boano, and K. Römer. Switchable Directional Antenna System for UWB-based Internet of Things Applications. In International Conference on Embedded Wireless Systems and Networks (EWSN), 2017

18  M. Rath, J. Kulmer, M. S. Bakr, B. Großwindhager and K. Witrisal, "Multipath-assisted indoor positioning enabled by directional UWB sector antennas," 2017 IEEE 18th International Workshop on Signal Processing Advances in Wireless Communications (SPAWC), Sapporo, 2017, pp. 1-5.